Proceedings of the ASME 2020 Conference on Smart Materials, Adaptive Structures and Intelligent Systems
SMASIS2020
September 14-16, 2020, Irvine, CA, USA

SMASIS2020-18247

FLOW CONTROL AND SEPARATION DELAY IN MORPHING WING AIRCRAFT USING TRAVELING WAVE ACTUATION

A. Olivett, P. Corrao, M.A. Karami
Department of Mechanical and Aerospace Engineering, University at Buffalo, SUNY
Buffalo, NY 14260, USA

ABSTRACT

This study examines the biomimicry of wave propagation, a mode of locomotion in aquatic life for the use-case of morphing aircraft surfaces for boundary layer control. Such motion is theorized to inject momentum into the flow on the upper surface of airfoils, and as a consequence, creates a forcible pressure gradient thereby increasing lift. It is thought that this method can be used to control flow separation and reduce likelihood of stall at high angles of attack. The motivation for such a mechanism is especially relevant for aircraft requiring abrupt maneuvers, and especially at high angles of attack as a safety measure against stalling. The actuation mechanism consists of lightweight piezoelectric ceramic transducers placed beneath the upper surface of an airfoil. An open-loop system controls surface morphing. A two-dimensional Fourier Transform technique is used to estimate traveling to standing wave ratio, which is verified analytically using Euler Bernoulli beam theory, and experimentally using a prototype wing. Propagating wave excitations are tuned and verified using a series of scanning laser vibrometry tests. A custom two-dimensional NACA 0018 airfoil tests the concept in a low-speed wind tunnel with approximate Reynolds Number of 50,000. Both traveling waves and the changes in lift and drag will be experimentally characterized.

INTRODUCTION

Morphing wings have received some attention in recent years as inventors are trying to improve the traditional wing in terms of efficiency and maneuverability. Unlike vernacular flaps, slats and ailerons, proposed morphing wing mechanisms are able to reconfigure shape through spatially continuous deformations. The general goal for morphing wing aircraft is to adapt to mission or maneuver-specific requirements rapidly and optimally without geometric or weight compromise imposed by traditional hydraulic actuators and linkage mechanisms. A review of morphing wings up to 2010 can be found in [1].

A problem that arises in flight that some morphing wing inventors are attempting to overcome is flow separation. Separated flow occurs at high angles of attack and can cause significant losses of energy [2]. If flow becomes fully separated aerodynamic stall will result. It is correlated with low Reynolds numbers flow, so researchers are soundly concerned with mitigating flow separation over small or low-speed unmanned aerial vehicles [3].

As flow separates, lift is diminished and drag is increased. This occurs for two reasons: the first being loss of a vertical pressure gradient, and the second, a reverse flow caused by the eddying separation bubble. If fluid viscosity, or Reynolds number is kept constant, laminar flow separation is dependent only on angle of attack. Partial separation near the leading edge begins forming at moderate angles of attack, and expands towards the trailing edge with steeper angles. Because the dynamics are nonlinear, flow during the occurrence of stall will exhibit hysteresis [4], in which recovery will only occur at much lower angles of attack. In short, mitigating flow separation is of great importance for two reasons 1.) avoidance of threatening stall at high angles of attack or low speed, and 2.) energy saving at moderate or low angles of attack.

Copyright © 2020 by ASME

Flow separation can be mitigated by decreasing angle of attack, increasing velocity, or having a more efficient wing. Wing efficiency can be improved by directly manipulating airflow adjacent to the surface – something known as boundary layer control. A survey of boundary layer control methods finds both active and passive devices. An early success was presented by Prandtl, himself responsible for introducing the concept of boundary layers – using suction to eliminate separation [2]. Other successful active methods are blowing [5], periodic synthetic jets [6], periodic excitation [7], and periodic surface morphing [8]. Passive methods are far more ubiquitous, and are as simple and practical as slots that pass through the wing [9], or vortex generators [10] that attach to the leading edge of a wing. Another proven method is moving surface boundary layer control (MSBC). This is the concept at play when a pitcher throws a baseball with a spin on it, causing more lift in this or that direction. In airfoil experiments, MSBC has increased lift coefficient as high as 100%, and delayed of stall angle as much as 400% [11]. Although promising, MSBS was never integrated into aircraft wings because the mechanisms used were impractical, consisting of rotating drums [11], or belts and pulleys mounted on airfoil surfaces [12].

The morphing wing presented in this paper is the product of a number of contributions from present and previous students of M.A. Karami's research group at University at Buffalo, and I. Borazjani's group at Texas A&M University. The idea was inspired by earlier morphing wings that use actuators for airfoil changing [13], [14]. It was proposed that multiple actuators along the surface of an airfoil with sinusoidal forcing would enable vibrational travelling waves – this idea was developed with the supposition that continuous travelling waves generated by low-profile actuators could facilitate MSBC within a practical mechanism. A procedure for generating and validating elastic travelling wave patterns was developed by Bani-Hani and Karami in 2015 for a swimming smart robot [15]. In 2017 P. Corrao built the first working morphing wing prototype, and it has served as a testbed for students since then. Akbarzadeh and Borazjani have shown promising results in numerical simulations [16], [17], [18]. In [17] it was shown that traveling waves over inclined plates can suppress stall and decrease drag by up to 75%. Importantly, their results quantitatively suggest that backward travelling waves are more effective than forward travelling or standing waves, because they accelerate adjacent fluid in the streamwise direction creating a propelling force similar to how fish swim.

Now, motivation aside, one should consider the morphing mechanism that generates vibrational travelling waves – it is a difficult problem in itself for several reasons. Since bending waves are dispersive, wave speed is not consistent but dependent on frequency. Further, waves in finite media will consistently reflect at the ends – forward and backward travelling waves in superposition will result in a standing wave [19]. A review of travelling wave methods [20] reveals that there are many compelling devices that overcome these problems. They include closed-loop strategies based on adaptive feedforward control [21], or active feedback control [22] – as well as open loop devices such as two-mode excitation [23], and acoustic black hole termination [24]. For this prototype, two-mode excitation was favored for its straightforwardness and easy setup. Closed-loop strategies are promising, but could be overly complicated for the initial proof-of-concept. They will most likely be favored in future studies for improved robustness and time saving – two-mode excitation as documented in later sections is a very time-consuming procedure.

This paper was written to document work from the past several years beginning with conceptual design and fabrication. Later sections cover analytical modeling of morphing dynamics, travelling wave tuning and verification procedures, laser vibrometer experiments, and preliminary wind tunnel tests.

1.1 PROTOTYPE DESIGN AND FABRICATION

Early and later designs for the morphing wing are illustrated in figure 1. Conceptually, the mechanism is driven by the actuator, which generates a bending wave from the leading edge towards the trailing edge. The counter-actuator is driven at the same frequency, but offset phase, and cancels-out reflected waves.

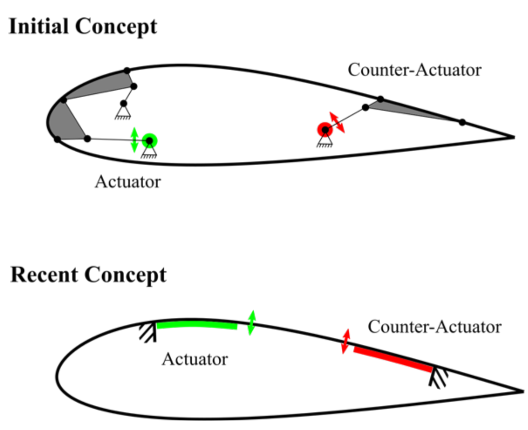

FIGURE 1: CONCEPTUAL ILLUSTRATIONS OF EARLY AND RECENT MORPHING MECHANISMS

Copyright © 2020 by ASME

The experimental prototype, shown prior to assembly in figure 2 uses a 0.002” thick spring steel morphing skin actuated by Mide PPA-1022 piezoelectric actuators, which were bonded to the skin with epoxy-resin in a vacuum bag. The actuated section covers 2.5 inches of the 12-inch span. The body of the wing was made by layering balsa wood and polystyrene, and adhered using Wood Glue. Polystyrene was cut using hot nichrome wire. The skin was attached to the wing with JB-Weld Two Part Epoxy.

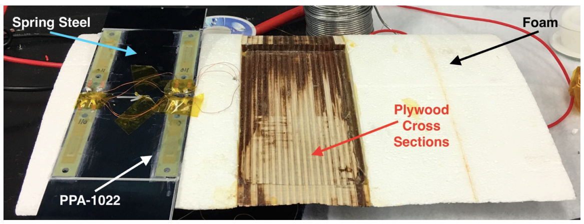

FIGURE 2: DISASSEMBLED MORPHING WING

Matching actuators were wired in parallel and connected to the external voltage supply through a small hole in the bottom of the wing. An analog control signal was generated by a National Instruments NI-USB-6002 DAQ, set up in LabVIEW. This signal was brought up to the necessary voltage amplitude using two Trek 2205 voltage amplifiers with 50 V/V gain. Figure 3 visualizes the electrical hardware setup.

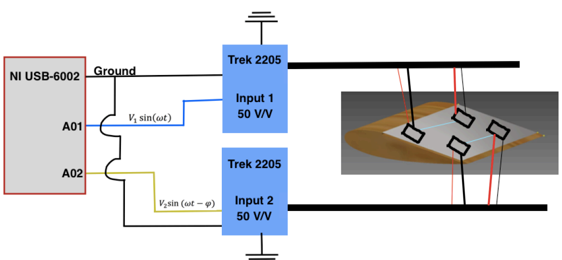

FIGURE 3: ELECTRICAL SCHEMATIC

1.2 MODELING PROCEDURE

Our model of vibrational travelling waves makes use of simplified one-dimensional dynamics. The simplified geometry, represented in figure 4 supposes that the entire morphing section behaves as a uniform composite beam with one actuator at the leading-edge and one at the trailing-edge. The equations presented here are more or less guided by the methods in [15], which models travelling waves of a robotic swimmer.

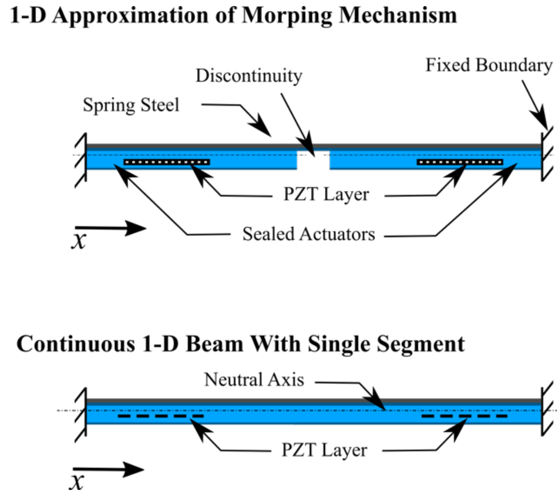

FIGURE 4: SIMPLIFIED GEOMETRY OF PIEZOELECTRIC MORPHING SURFACE

One-dimensional bending deflections may be modeled using the Euler-Bernoulli beam model [25], which is summarized by the following partial differential equation:

$$c^2 \frac{\partial^4 w}{\partial x^4}(x,t) + \frac{\partial^2 w}{\partial t^2}(x,t) = 0 \qquad (1)$$

Where $c = \sqrt{\frac{YI}{\rho A}}$, Y is young’s modulus, I is moment of inertia, ρ is density, A is area, w is deflection, and x and t are spatial and temporal variables. When a piezoelectric actuator is introduced for bending, electromechanical dynamics are given by the two governing equations [26]:

Mechanical:

$$YI \frac{\partial^4 w}{\partial x^4}(x,t) + \rho A \frac{\partial^2 w}{\partial t^2}(x,t) - \frac{d^2}{dx^2}(v(t)\alpha) \qquad (2)$$

Electrical:

$$c_o v(t) = -\int_0^L \alpha \frac{\partial^2 w}{\partial x^2}(x,t)dx \qquad (3)$$

Where: $\alpha = -d_{31} Y_p b_p (h_{pt}^2 - h_{pb}^2)/2h_p$ is the driving constant. $v(t)$ is voltage signal, c_o is capacitance, d_{31} is the piezoelectric constant, Y_p is piezoelectric modulus, b_p is width of the actuator, h_p is height of the actuator, and h_{pt} and h_{pb} are distances from the neutral axis to the top and bottom of the actuator respectively. The bending moment introduced by the actuator, $\frac{d^2}{dx^2}(d_{31} v z_m b)$ is approximated with Heaviside functions evaluated at the two ends of the actuator, x_1 and x_2.

Copyright © 2020 by ASME

$$M = YI\frac{\partial^2 w}{\partial t^2}(x,t) + \cdots \\ \alpha v(t)[H(x-x_1) - H(x-x_2)] \quad (4)$$

To arrive at equation (5), it is useful reminder that the second derivative of the Heaviside function, $H''(x)$ is the first derivative of the delta function, $\delta'(x)$. Given these considerations, the mechanical governing equation is reevaluated as:

$$YI\frac{\partial^4 w}{\partial x^4}(x,t) + \rho A\frac{\partial^2 w}{\partial t^2}(x,t) + \cdots \\ \alpha v(t)[\delta'(x-x_1) - \delta'(x-x_2)] \quad (5)$$

Assuming dynamics are linear, equation (4) may be solved using separation of variables technique and eigenvalue decomposition, whereby the response is represented as an infinite series of orthogonal mode-shapes, $W_j(x)$ corresponding second order temporal responses, $\eta_j(t)$. Equation (6) is the separated solution in modal coordinates.

$$w(x,t) = \sum_{i=1}^{\infty} W_i(x)\,\eta_i(t) \quad (6)$$

The undamped modal response is defined for each actuator in equations (7) and (8) – LE represents the leading-edge actuators and TE represents trailing-edge actuators.

$$\sum_{j=1}^{\infty} \ddot{\eta}_{jLE} + \omega_j^2 \eta_{jLE} = k_{jLE} v(t) \quad (7)$$
$$\sum_{j=1}^{\infty} \ddot{\eta}_{jTE} + \omega_j^2 \eta_{jTE} = k_{jTE} v(t) \quad (8)$$

Where: $k_{jLE} = \alpha\left[W_j'(L_1) - W_j'(0)\right]$
$k_{jTE} = \alpha\left[W_j'(L) - W_j'(L_2)\right]$
$v_{LE}(t) = A\sin(\omega_{act} t + \phi_{LE})$
$v_{TE}(t) = A\sin(\omega_{act} t + \phi_{TE})$

The steady-state output (10) for a sinusoidal driving voltage was evaluated using the transfer function (9). This was computed for each modal coordinate and multiplied by corresponding mode-shapes. Finally, in accordance with equation (6), total response is the sum of all products for every actuator.

$$T = \frac{k_j}{\omega_j^2 - \omega_{act}^2} A \quad (9)$$
$$\eta_j = |T|\sin(\omega_{act} t + \phi + \phi_{TF}) \quad (10)$$

Where $|T|$ is absolute amplitude of T and ϕ_T is the phase angle of T.

The frequency function of a beam is defined by its boundary conditions. Suppose that dimensionless frequency β is the independent variable, and the matrix $M(\beta)$ contains all of equations representing boundary conditions. The beam's natural frequencies appear where $M(\beta)$ evaluates to zero, and as such the frequency function is defined in equation (12).

$$f(\beta) = \det(M(\beta)) \quad (12)$$

Where: $\beta = \left(\frac{\omega^2}{c^2}\right)^{1/4} = \left(\frac{\rho A \omega^2}{EI}\right)^{1/4}$

This can be solved using a gradient search type method so long as there are valid initial guesses – these can be found by calculating the determinant over a rough distribution of β values and detecting changes in $sign\{f(\beta)\}$ – a method which indispensable if a segmented beam approach is taken and there are 6 or 8 boundary conditions instead of the usual 4.

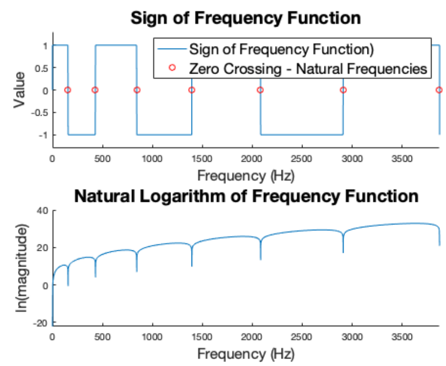

FIGURE 5: FREQUENCY FUNCTION

The solution for mode-shapes $W_j(x)$ is defined by equation (13), where $C_{1,n}$ through $C_{4,n}$ are the coefficients. Figure 5 graphically represents the frequency function, while figure 6 shows the mode-shapes.

$$W_j(x) = C_{1,j}\sin(\beta_j x) + C_{2,j}\cos(\beta_j x) + \\ C_{3,j}\sinh(\beta_j x) + C_{4,j}\cosh(\beta_j x) \quad (13)$$

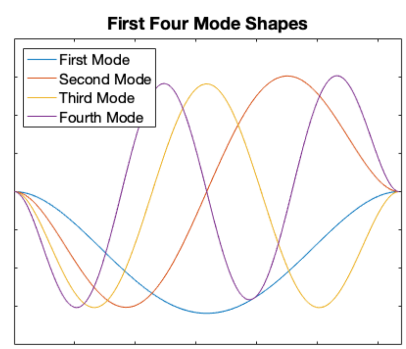

FIGURE 6: MODE SHAPES OF FIX-FIX BEAM

 Copyright © 2020 by ASME

1.3 COMPUTATIONAL TRAVELING WAVE RESULTS

A series of simulations were run consecutively and assigned traveling to standing wave ratio indexes (TSR), based on the 2D FFT method used in [15]. The goal was to maximize TSR ($0 \leq TSR \leq 1$). This was carried out using the built-in MATLAB gradient search function fmincon [27], with trailing edge actuator phase, ϕ_{LE} as the independent variable. The general framework for this process is illustrated in figure 7.

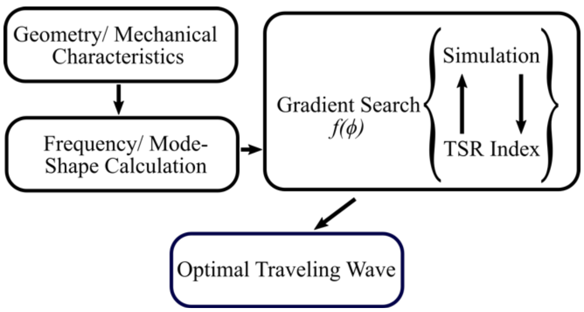

FIGURE 7: COMPUTATIONAL PROCEDURE

A typical waveform has both standing and travelling components. When a standing wave overtakes a travelling wave the nodes of the mode-shape become pronounced. The two-mode excitation method suggests that a travelling wave can be generated if two actuators are present on a beam, by mixing two adjacent modes, and delaying the phase of one actuator by 90˚. As actuating frequency converges towards the natural frequencies, vibrational mode-shapes dictate dynamics and only standing waves are possible. Because of this, a typical actuating frequency is the average of two adjacent natural frequencies, and the initial guess for trailing edge phase is always around -90˚.

Figures 8 & 9 show the wave envelope and 2D FFT for a perfect standing wave, and figures 10 & 11 show the same graphics for an optimal travelling wave. Equation (13) gives the relationship for TSR, which is defined as the ratio of peaks in adjacent quadrants on the 2D FFT Surface. Intuitively, eliminating peaks in these quadrants can be thought of as eliminating the positive – or conversely the negative frequency component, leaving waves travelling in only one direction.

$$TSR = \frac{\max(fft_{1st}) - \max(fft_{3rd})}{\max(fft_{1st})} \tag{13}$$

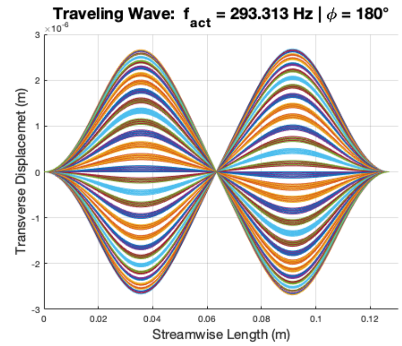

FIGURE 8: ENVELOPE OF STANDING WAVE

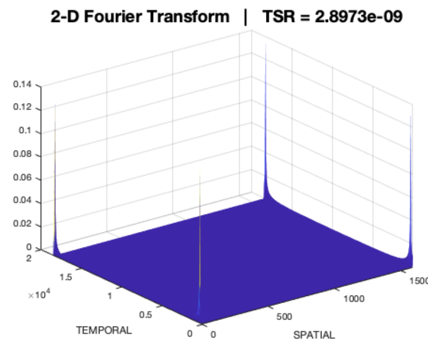

FIGURE 9: 2D FFT OF STANDING WAVE

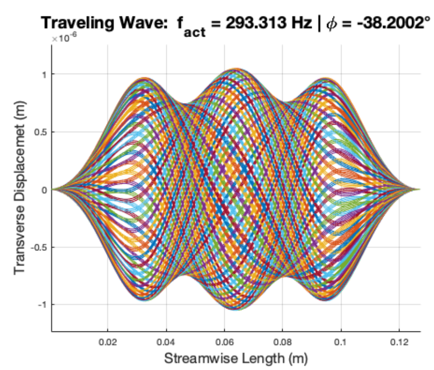

FIGURE 10: ENVELOPE OF OPTIMAL TRAVELING WAVE

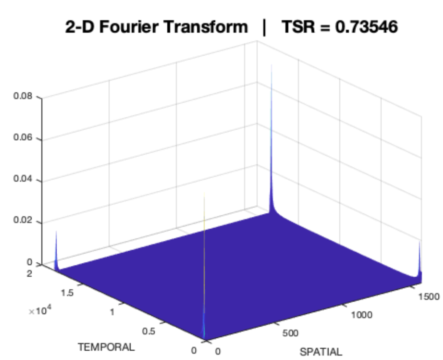

FIGURE 11: 2D FFT OF OPTIMAL TRAVELING WAVE

Copyright © 2020 by ASME

1.4 EXPERIMENTAL TRAVELING WAVE RESULTS

To validate traveling waves experimentally it is necessary to have spatial and temporal data of the actuated section's motion. The equipment used was a Polytec PSV-500 Laser Doppler Vibrometer with scanning capability – courtesy of Dr. Mostafa Nouh, the equipment belongs to the Sound and Vibrations Laboratory at University at Buffalo. Figure 12 shows the experimental setup. Reflective tape was attached to the morphing surface to enhance the laser signal.

FIGURE 12: POLYTEC PSV-500 SCANNING HEAD WITH MODEL IN BACKGROUND

The tuning process consisted of choosing base frequencies and adjusting frequency in increments of 5˚, and trailing-edge actuator phase in increments of 10˚. The optimal traveling waves found through this process are shown in figures 13 and 14.

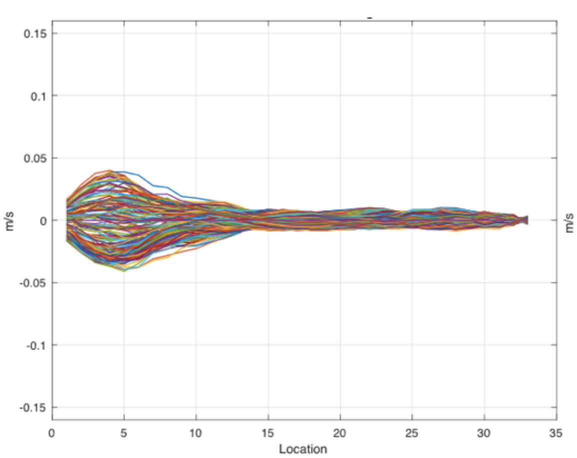

FIGURE 13: ENVELOPE FOR 167 HZ TRAVELING WAVE

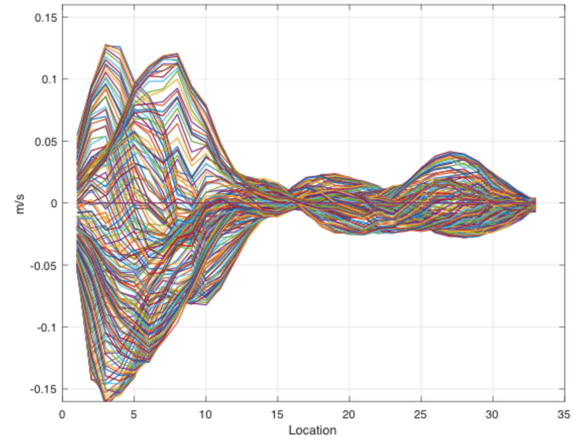

FIGURE 14: ENVELOPE FOR 200 HZ TRAVELING WAVE

1.5 LIFT AND DRAG EXPERIMENTS

Lift and drag experiments were conducted in the Department of Mechanical and Aerospace Engineering's teaching wind tunnel at University at Buffalo. It is a low-speed open-loop tunnel manufactured by Engineering Laboratory Design Inc. The test area is 24 inches long, with a 12-inch square cross-section. Airspeed is interpreted by a single pitot tube which can be lifted out of the test area after velocity is recorded. Lift and Drag are measured with a force balance supporting the wing with a vertical sting. Angle of attack (AOA) is adjusted manually. The setup for these experiments is shown in figures 15 and 16.

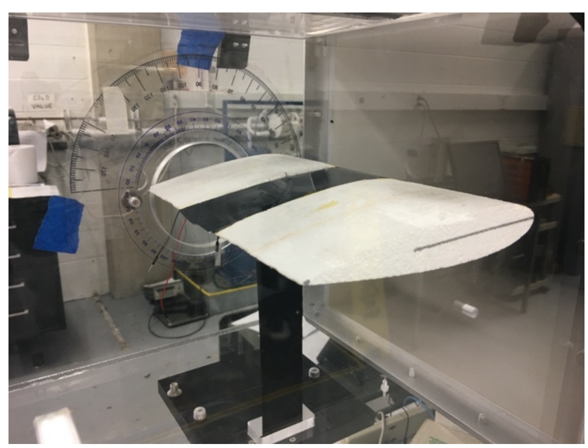

FIGURE 15: MORPHING WING MODEL IN TEST SECTION

Copyright © 2020 by ASME

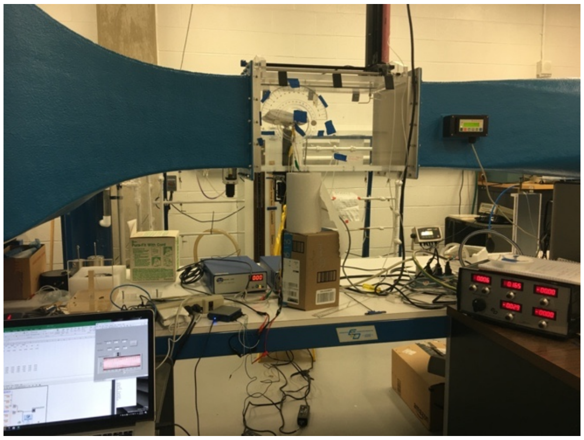

FIGURE 16: TEST AREA AND DATA ACQUISITION

The experiments were carried out with a free stream velocity of 5.31 m/s, which in using equation (14) with the chordwise dimension is a flow with Reynolds number approximately 50,000. A number of actuation frequencies were experimented with, summarized in table 1. Each actuation frequency was tested at a range of AOA. Only the experiments at 167 Hz and 200 Hz were traveling waves. The other frequencies were arbitrary standing waveforms with frequencies corresponding to optimal reduced frequencies that Greenblatt and Wygnanski suggested from experiments with periodic excitation flow control [7]. They were meant to serve as a useful comparison. Reduced frequency F^+ is given by equation (15). Lift and drag curves in figures 17 & 18 summarize these experiments.

$$Re = \frac{\rho_{air} U_\infty L}{\mu_{air}} \tag{14}$$

$$F^+ = \frac{f_{act} X_{TE}}{U_\infty} \tag{15}$$

Where ρ_{air} is density of air, U_∞ is free stream velocity, L is chord length, μ_{air} is dynamic viscosity, f_{act} is actuation frequency, and X_{TE} is distance from excitation location to trailing edge.

Frequency (Hz)	Waveform Pattern
0	None
12	Standing
78	Standing
167	Travelling
200	Travelling

TABLE 1: SUMMARY OF ACTUATION USED IN WIND TUNNEL EXPERIMENTS

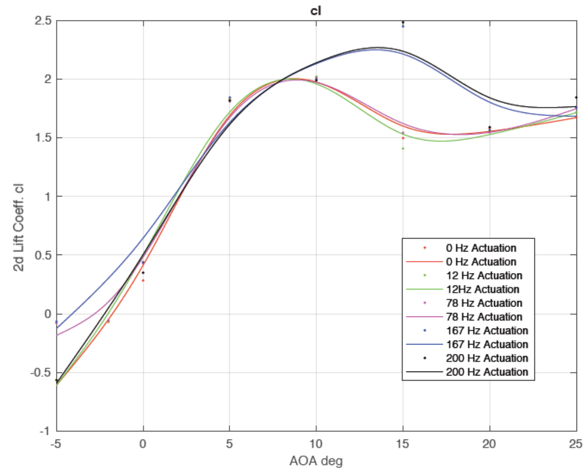

FIGURE 17: LIFT DATA WITH SPLINE FITTING

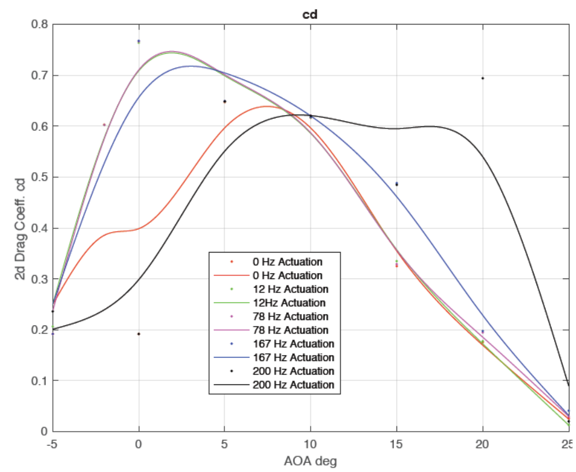

FIGURE 18: DRAG DATA WITH SPLINE FITTING

1.6 DISCUSSION

In figure 17, static stall occurs at about 10˚ AOA. It is clear from this representation of the data that travelling waves at 167 Hz and 200 Hz are effective at delaying stall to at least 15˚ AOA. Where stall is delayed, the enhancement in lift coefficient compared with no actuation is as much as 66%. The standing waveforms at 12 Hz, and 78 Hz offer no apparent improvements in efficiency – this of course, cannot in itself totally discredit their effectiveness, or for that matter the work in [7]. This morphing wing is a new and different type of mechanism. Also, since measurements were taken in increments of 5˚ AOA, the standing waves very well could have delayed stall several degrees without being recorded. Nonetheless, it is objective to say that the traveling waves in this study were certainly more effective at delaying stall than the standing waves.

Figure 18 shows the drag data, which is more difficult to interpret. The 167 Hz traveling wave drag

 Copyright © 2020 by ASME

curve is very distinct form the 200 Hz traveling wave drag curve. The 167 Hz traveling wave, along with both standing waves have a net positive effect on drag (compared with no actuation) before separation, and a net negative effect on drag after separation. The opposite could be said for the 200 Hz traveling wave, which decreases drag before separation and increases drag after separation. Interestingly, all measurements converge at 10˚, and both traveling waves affect drag equally when they delay separation at 15˚ AOA, where drag coefficient is increased by as much as 50%.

It is difficult to come to a decisive conclusion when considering these drag results. The question remaining is why two different traveling waves affect drag coefficient in totally different ways. A possible explanation is that wave-speed and wavelength make the difference. Because bending waves are dispersive, the 200 Hz wave is of a higher velocity than the 167 Hz one. This could be related to the conclusion reached in Akbarzadeh and Borazjani's study of an inclined plate with traveling waves. They note that increased velocity will delay flow separation, increase lift, and decrease drag – however, wavelength will not have a monatomic effect. They conclude that both frequency and wavelength individually impact the flow separation [17]. But applying this explanation is not even close to enough to resolve this complicated issue – visual inspection of figure14 shows that the 200 Hz traveling wave has a very strong standing wave component near the leading edge, and is of a much higher amplitude than the 167 Hz wave in figure 13. Waveform amplitude or TSR may have unprecedented nonlinear effects on the flow. Furthermore, since the distribution of data is very rough, the perceived disparity between the two traveling waves could very well have come from a misleading error in data acquisition. Regardless, it will be made sure that future studies are to have more data samples across AOA, and more attention will be focused on controlling parameters such as amplitude, TSR, and wave speed.

1.7 CONCLUSION

The successes presented here include construction of a working prototype, an electromechanical model capable of optimal two-mode excitation, experimental two-mode traveling waves, and validation of flow separation control through preliminary wind tunnel results.

ACKNOWLEDGEMENTS

- NSF Award # 1905252 | Collaborative Research: Controlling Flow Separation via Traveling Wave Actuators
- Professor Mostafa Nouh and his students at University at Buffalo's sound and Vibrations Lab for their time and help and permission to use the Polytec Vibrometer.
- University at Buffalo's AIAA and SEDS student clubs for help with fabrication.
- Professor Iman Borazjani's group at Texas A&M University for insights and collaboration.
- Support from NSF, NIH, and SUNY Research Foundation.

REFERENCES

[1] S. Barbarino, O. Bilgen, R. M. Ajaj, M. I. Friswell and D. J. Inman, "A Review of Morphing Aircraft," *Journal of Intelligent Material Systems and Structures,* vol. 22, no. 9, pp. 823-877, 2011.

[2] P. K. Chang, Separation of Flow, Oxford: Pergamon Press, 1970.

[3] T. J. Muller and J. D. DeLaurier, "Aerodynamics of Small Vehicles," *Annual Review of Fluid Mechanics,* vol. 35, pp. 89-111, 2003.

[4] H. Hu, Z. Yang, H. Igarashi and M. Martin, "An Experimental Study of Stall Hysteresis of a Low-Reynolds-Number Airfoil," *International Journal of Aerospace and Lightweight Structures,* vol. 1, no. 2, pp. 221-238, 2011.

[5] J. K. Wimpress, "Upper Surface Blowing Technology as Applied to the YC-14 Airplane," *SAE Transactions,* vol. 82, no. 4, pp. 3049-3056, 1973.

[6] D. C. McCormick, "Boundary Layer Separation Control With Directed Synthetic Jets," *AIAA,* vol. 519, 2000.

[7] D. Greenblatt and I. J. Wygnanski, "The control of flow separation by periodic excitation," *Progress in Aerospace Sciences,* vol. 36, pp. 487-545, 2000.

[8] G. Jones, M. Santer, M. Debiasi and G. Papadakis, "Control of flow separation around an airfoil at low Reynolds numbers using periodic surface morphing," *Journal of Fluids and Structures,* vol. 76, pp. 536-557, 2018.

[9] M. Ramzi and G. AbdErrahmane, "Passive Control via Slotted blading in a Compressor Cascade at Stall Condition," *Journal of*

 Copyright © 2020 by ASME

Applied Fluid Mechanics, vol. 6, no. 4, pp. 571-580, 2013.

[10] J. C. Lin, "Review of research on low-profile vortex generators to control boundary-layer separation," *Progress in Aerospace Sciences,* vol. 38, pp. 389-420, 2002.

[11] V. J. Modi, "Moving surface boundary-layer control," *Journal of Fluids and Structures,* vol. 11, pp. 627-663, 1997.

[12] E. Salimipour and S. Yazdani, "Improvement of aerodynamic performance of an offshore wind turbine blad by moving surface mechanism," *Ocean Engineering,* vol. 195, 2020.

[13] H. P. Monner, M. Kinstscher, T. Lorkowski and S. Storm, "Design of a Smart Droop Nose as Leading Edge High Lift System for Transportation Aircrafts," in *50th AIAA/ASME/AHS/ASC Strucural Dynamics, and Materials Conference*, Palm Springs, CA, 2009.

[14] S. Vasista, J. Riemenschneider, R. Keimer, H. P. Monner, F. Nolte and P. Horst, "Morphing Wing Droop Nose with Large Deformation: Ground Tests and Lessons Learned," *MDPI Aerospace,* 2019.

[15] M. A. Bani-Hani and M. A. Karami, "Analytical structural optimization and experimental verifications for traveling wave generation in self-assembling swimming smart boxes," *Smart Materials and Structures,* vol. 24, no. 094005, 2015.

[16] A. Akbarzadeh and I. Borazjani, "A numerical study on controlling flow separation via surface morphing in the form of bakward travelling waves," in *AIAA Aviation 2019 Forum*, Dallas, Texas.

[17] A. M. Akbarzadeh and I. Borazjani, "Reducing flow separation of an inclined plate via travelling waves," *Journal of Fluid Mechanics,* vol. 880, pp. 831-863, 2019.

[18] A. M. Akbarzadeh and I. Borazjani, "Large eddy simulations of a turbulent channel flow with a deforming wall undergoing high steepness," *Physics of Fluids,* vol. 31, no. 12, p. 125107, 2019.

[19] L. E. Kinsler, A. R. Frey, A. B. Coppens and J. V. Sanders, Fundamentals of Acoustics, Fourth Edition, New York: John Wiley & Sons, Inc., 2000.

[20] R. Gabai and I. Bucher, "Excitation and sensing of multiple vibrating traveling waves in one-dimensional structures," *Journal of Sound and Vibration,* vol. 319, pp. 406-425, 2009.

[21] S. J. Elliott and L. Billet, "Adaptive Control of Flexural Waves Propagating in a Beam," *Journal of Sound and Vibration,* vol. 163, no. 2, pp. 295-310, 1992.

[22] D. J. Pines and A. H. von Flowtow, "Active Control of Bending Wave Propagation," in *IEEE 1989 American Control Conference*, Pittsburgh, PA, 1981.

[23] P. I. Ro and B.-G. Loh, "An Object Transport System Using Flexural Ultrasonic Progressive Waves Generated by Two-Mode Excitation," *IEEE Transactions on Ultrasonics, Ferroelectrics, and Frequency Control,* vol. 47, no. 4, pp. 994-999, 2000.

[24] V. Denis, F. Gautier, A. Pelat and J. Poittevin, "Measurement and modelling of the reflection coefficient of an Acoustic Black Hole termination," *Journal of Sound and Vibration,* vol. 349, pp. 67-79, 2015.

[25] S. S. Rao, Vibration of Continuous Systems, Second Edition ed., Hoboken, NJ: Wiley, 2019.

[26] O. Bilgen, M. A. Karami, D. J. Inman and M. I. Friswell, "The actuation characterization of cantilevered unimorph beams with single crystal piezoelectric materials," *Journal of Vibration and Acoustics,* vol. 20, no. 055024, 2011.

[27] Mathworks, "Help Center fmincon," [Online]. Available: mathworks.com/help/optim/ug/fmincon.

 Copyright © 2020 by ASME